Heliyon 10 (2024) e36415

Contents lists available at ScienceDirect

Heliyon

journal homepage: www.cell.com/heliyon

Research article

Nuclear translocation of nucleotide enzyme Phosphoglucomutase 2 governs DNA damage response and anti-tumor immunity☆

Yingying Lyu [a,1], Chaxian Liu [a,1], Hao Lin [a,1], Haikun Song [d], Qiyuan Zhuang [a], Ankang Hu [a], Liang Chen [a,b,c,e,**], Hui Yang [a,b,c,d,e,***], Ying Mao [a,b,c,e,2,*]

[a] Department of Neurosurgery, Huashan Hospital, Fudan University, Shanghai, PR China
[b] National Center for Neurological Disorders, Huashan Hospital, Fudan University, Shanghai, PR China
[c] Shanghai Key Laboratory of Brain Function Restoration and Neural Regeneration, Huashan Hospital, Fudan University, Shanghai, PR China
[d] Institute for Translational Brain Research, Shanghai Medical College, Fudan University, Shanghai, PR China
[e] State Key Laboratory of Medical Neurobiology and MOE Frontiers Center for Brain Science, Institutes of Brain Science, Fudan University, Shanghai, PR China

ARTICLE INFO

Keywords:
Glioblastoma
Nucleotide metabolism
Anti-tumor immunity
Non-canonical function
DNA damage
PGM2
ROCK2

ABSTRACT

Targeting nucleotide enzymes emerges as a promising avenue for impeding tumor proliferation and fortifying anti-tumor immunogenicity. The non-canonical role of nucleotide enzymes remains poorly understood. In this study, we have identified that Phosphoglucomutase 2 (PGM2) rapidly accumulates at the DNA damage site to govern the DNA damage response mediated by the phosphorylation at Serine 165 and by forming a complex with Rho-associated coiled-coil-containing protein kinase 2 (ROCK2). Silencing PGM2 in Glioblastoma Multiforme (GBM) cells heightens DNA damage in vitro and enhances the sensitivity of temozolomide (TMZ) treatment by activating anti-tumor immunity in vivo. Furthermore, we demonstrate that pharmacological inhibition of ROCK2 synergistically complements TMZ treatment and pembrolizumab (PD-L1) checkpoint immunotherapy, augmenting anti-tumor immunity. This study reveals the non-canonical role of the nucleotide enzyme PGM2 in the regulation of DNA damage response and anti-tumor immunity, with implications for the development of therapeutic approaches in cancer treatment.

1. Introduction

GBM, a malignant tumor with a poor prognosis and limited treatment options, primarily relies on traditional chemotherapy and radiation therapy as standard treatments while facing significant challenges in the context of immunotherapies [1]. Even with optimal treatment, recurrence remains almost inevitable in the majority of cases [2]. GBM is also known as a "cold tumor" due to its

☆ The authors have declared that no conflict of interest exists.

* Corresponding author.
** Corresponding author.
*** Corresponding author. Department of Neurosurgery, Huashan Hospital, Fudan University, Shanghai, PR China.
E-mail addresses: chenlianghs@126.com (L. Chen), hui_yang@fudan.edu.cn (H. Yang), maoying@fudan.edu.cn (Y. Mao).
[1] These authors contributed equally to this work.
[2] Lead Contact.

https://doi.org/10.1016/j.heliyon.2024.e36415
Received 26 March 2024; Received in revised form 1 August 2024; Accepted 15 August 2024
Available online 26 August 2024

insensitivity to immunotherapies. GBM cells acquire distinctive metabolic characteristics that facilitate their rapid proliferation and treatment resistance [3]. One such trait is the manipulation of nucleotide metabolism, which is pivotal in conferring resistance to cancer therapies [4]. The augmented nucleotide metabolism permits the aggressive behaviors of GBM cells including the immune evasion of GBM cells [4]. Considerable attention has been directed toward unraveling the nucleotide metabolism intricacies in glioma cells, particularly within the pyrimidine and purine pathways [5,6]. Nucleotide imbalance and nucleoside degradation regulate cell state transitions and cell fate decisions, particularly following replication stress [7]. The nucleotide metabolism greatly affects the DNA repair and therapy resistance in GBM by increasing nucleobase-containing metabolites and the inhibition of nucleotide synthesis enzymes sensitizes GBM cells to radiation therapy [8]. Therefore, targeting nucleotide metabolism and DNA damage repair in GBM represents a potential strategy for sensitizing GBM to treatments. Recent research has demonstrated that aberrations in nucleotide metabolism not only affect tumor development, but also disrupt the typical immune response within the tumor microenvironment (TME), highlighting the potential for targeting nucleotide metabolism as a way to enhance immunotherapeutic interventions [9].

The concept of metabolic enzymes performing additional, non-canonical ("moonlighting") functions has attracted considerable attention in recent years. Beyond their established roles as enzymes, numerous metabolic enzymes and metabolites exhibit non-canonical functions that support the malignant transformation of cancer cells [10]. Classic enzymes such as glyceraldehyde-3-phosphate dehydrogenase (GAPDH) [11], phosphoglycerate mutase 2 (PGAM2) [12], and pyruvate kinase M2 (PKM2) [13] are known to possess important non-canonical roles.

PGM2 is a component of the pentose phosphate pathway (PPP) and its role in cancer cells remains inadequately elucidated. The PPP, which operates in parallel to glycolysis, generates NADPH, pentoses, and ribose-5-phosphate (R-5-P), a precursor necessary for nucleotide synthesis to support DNA replication and DNA damage repair [14]. The canonical function of PGM2 lies in catalyzing the conversion of ribose-1-phosphate and deoxyribose-1-phosphate, which are the breakdown products of nucleosides, into their respective 5-phosphopeptides. This enzymatic activity facilitates the recycling of degradation products, enabling their incorporation into subsequent nucleotide synthesis processes [15].

In this study, we found that the cytoplasmic PGM2 translocated into nuclear upon DNA damage drug treatment. Moreover, the nuclear PGM2 rapidly accumulates at DNA damage sites shortly after the occurrence of DNA double-strand breaks (DSBs), which depends on the phosphorylation of PGM2 at the Ser 165 site and the binding with ROCK2. Targeting PGM2 sensitizes GBM cells to chemotherapy and enhances the anti-tumor immunity in vivo. Our findings support that targeting PGM2 may be a promising strategy to overcome therapy resistance in GBM.

2. Results

2.1. PGM2 translocates into the nucleus by chemo-drug treatment

PGM2 was reported as primarily located in the cytoplasm involving in the ribose-phosphate conversion within the pentose phosphate pathway (Fig. 1A). Comprehensive investigation of the expression and localization of PGM2 within cancer cells has unveiled its dual residency, spanning both cytoplasmic and nuclear compartments, a discovery substantiated by endogenous PGM2 antibody staining (Fig. 1B–D; Fig. S1D). Further validation through the depletion of PGM2 using single-guide RNAs (sgRNAs) confirmed its presence in both the cytoplasm and nucleus of U251 cells (Fig. S1B). We next engineered PGM2 variants tagged with HA, Flag, and GFP, subjecting them to immunostaining, collectively verified the dual residency of PGM2 in the cytoplasm and nucleus (Fig. 1E; Figs. S1A and S1C and S1E-H). Together, these results conclusively establish that PGM2 is not confined to the cytoplasm but also locates the nucleus within cells.

To further investigate the signaling in controlling the localization of PGM2, we found the nuclear translocation of PGM2 was induced by the treatment of TMZ or doxorubicin (Doxo) in U251 (Fig. 1F and G). To further study the dynamic subcellular location change of PGM2, we subjected HeLa and U2OS cells stably expressing GFP-PGM2 or HA-PGM2 to TMZ, Doxo, and etoposide (Eto) treatment. Our results revealed a significant translocation of PGM2 into nuclear by chemo-drug treatment (Fig. 1J and K; Figs. S1G and H). Cytosolic and nuclear fractionation separation also confirmed that nuclear PGM2 level increased upon chemo-drug treatment (Fig. S1I). We observed the dynamic of nuclear translocation of GFP-PGM2 using living cell imaging with increased nuclear translocation upon Eto treatment in U2OS (Fig. 1H and I). We also observed the accumulation of PGM2 in the nucleus in G2/M checkpoint upon cell cycle blockade, consistent with its role in DNA damage repair (Figs. S1J and S1K). In summary, our data presents strong evidence for PGM2's dual presence within cancer cells, existing in both the cytoplasm and nucleus. Notably, we observed an enhanced nuclear localization of PGM2 under conditions of chemo-drug treatment. These insights shed light on the intricate interplay between PGM2 and DNA damage repair processes.

2.2. PGM2 depletion enhances the sensitivity of GBM cells to DNA damage

The dynamic relocation of PGM2 under chemo-drug treatment prompted us to further explore the function of PGM2 in DNA damage repair. Analysis of the TCGA database revealed significantly elevated expression of PGM2 in GBM (Fig. 2A). To gain deeper insights into the functional involvement of PGM2 within glioma cells, we used two independent sgRNAs to efficiently knockout PGM2 in U251 cells (Fig. 2B). Notably, our findings reveal a substantial increase in DNA damage levels in U251 cells lacking PGM2, both in the presence and absence of TMZ treatment, as evidenced by elevated levels of phospho-γH2A (Fig. 2C and D). Knockdown of PGM2 using shRNA also achieved consistent results (Figs. S2B and C). Additionally, the neutral comet assay revealed increased double-strand DNA break in PGM2 knockout cells (Fig. 2E and F). The depletion of PGM2 significantly sensitized U251 cells to TMZ treatment with

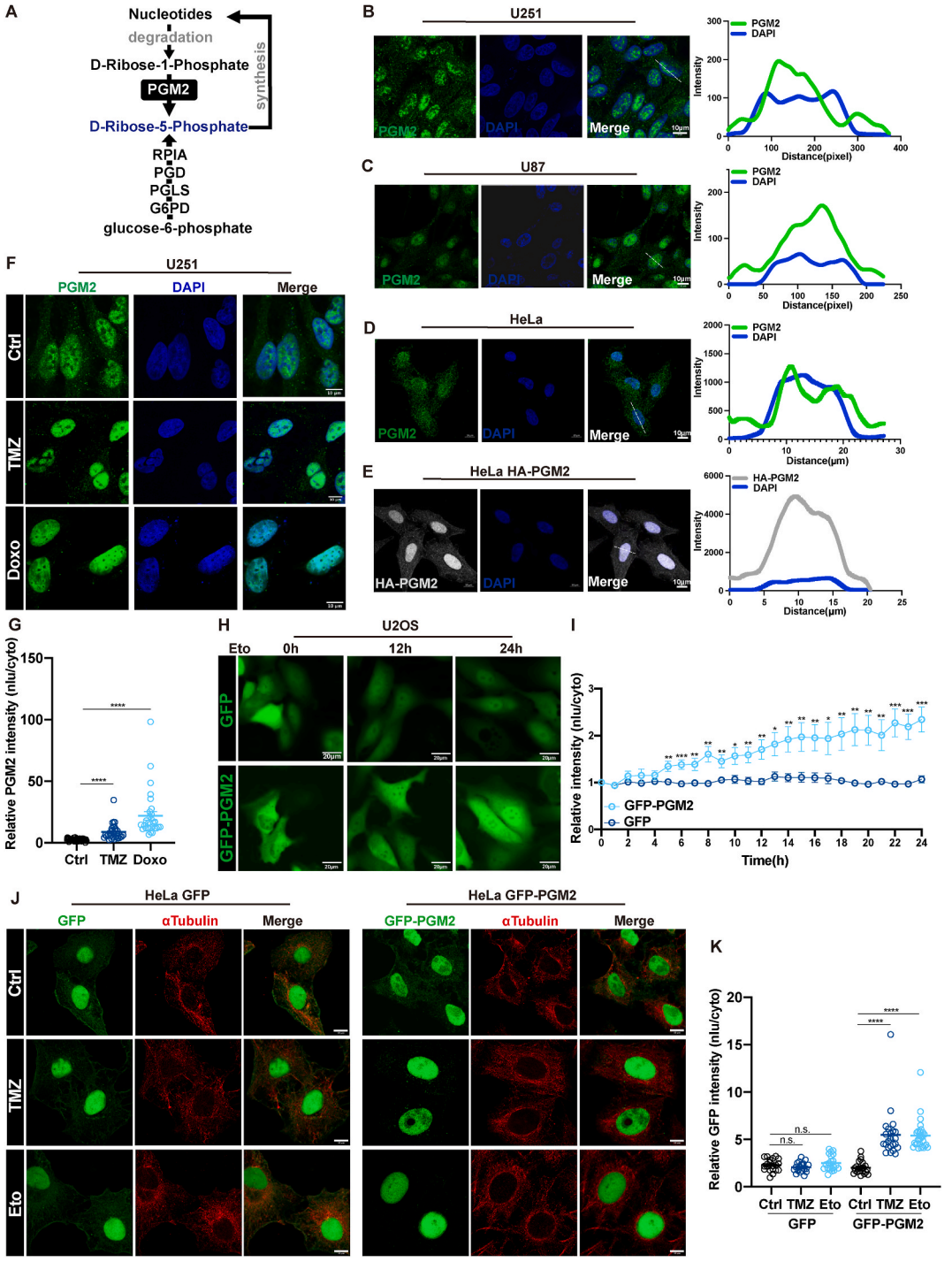

(caption on next page)

Fig. 1. PGM2 translocates into the nucleus by chemo-drug treatment. A. PGM2 functions in ribose-phosphate conversion. B. Immunofluorescence staining of endogenous PGM2 in U251 cells using PGM2 antibody and co-localization profiling of PGM2 with DAPI of line-indicated section. Scale bar: 10 μm. C. Immunofluorescence staining of endogenous PGM2 in U87 cells using PGM2 antibody and co-localization profiling of PGM2 with DAPI of line-indicated section. Scale bar: 10 μm. D. Immunofluorescence staining of endogenous PGM2 in HeLa cells using PGM2 antibody and co-localization profiling of PGM2 with DAPI of line-indicated section. Scale bar: 10 μm. E. Immunofluorescence staining of HA-tagged PGM2 in HeLa cells using HA antibody and co-localization profiling of PGM2 with DAPI of line-indicated section. Scale bar: 10 μm. F. Immunofluorescence images of PGM2 staining in ctrl, TMZ-treated, and Doxo-treated U251 cells, with nuclei counterstained by DAPI. U251 cells were treated with 0.001% DMSO, 400 μM TMZ, or 2 μM Doxo for 24 h. G. Quantification of PGM2 intensity (Nuclear intensity/Cytoplasmic intensity) in figure F. At least 30 cells were measured in each group. H. Representative images of live-cell imaging in U2OS cells. Scale bar: 20 μm. U2OS cells were transfected with GFP or GFP-PGM2, followed by live-cell imaging with or without 5 μM etoposide for 24 h. I. Quantification of relative GFP intensity (Nuclear intensity/Cytoplastic intensity) of live-cell imaging in U2OS cells, with 10 cells measured in each group. J. Immunofluorescence images displaying GFP or GFP-PGM2 and αTubulin in 0.001%DMSO-treated, TMZ-treated, and etoposide-treated HeLa cells, with nuclei counterstained by DAPI. HeLa cells were transfected separately with GFP or GFP-PGM2, and then treated with 0.001%DMSO, 400 μM TMZ, or 5 μM etoposide for 24 h. K. Quantification of relative GFP intensity (Nuclear intensity/Cytoplasmic intensity) of GFP or GFP-PGM2 in figure J. At least 20 cells were measured in each group. Statistical significance was denoted as * for $p < 0.05$, ** for $p < 0.01$, and *** for $p < 0.001$.

increased cell death (Fig. S2A). To further validate the role of PGM2 in DNA damage repair, we conducted immuno-staining assays targeting phospho-γH2A foci and TP53BP1 foci with and without TMZ treatment in U251. Our results demonstrate that PGM2 knockout leads to elevated DNA damage levels (Fig. 2G-J). Taken together, these findings unveil the role of PGM2 in the intricate machinery of DNA damage response and the depletion of PGM2 enhances the sensitivity of GBM cells to DNA damage.

2.3. Nuclear PGM2 is recruited to the DNA damage site

In order to determine the precise functional domain of PGM2 implicated in DNA damage repair, we conducted a meticulous investigation into the distinct roles played by cytoplasmic and nuclear PGM2 within PGM2-knockout HeLa and U2OS cells. To achieve this, we introduced distinct GFP-PGM2 constructs, each featuring nuclear localization sequences (NLS) and nuclear export sequences (NES) (Figs. S3A and B). The intracellular localization patterns were validated by the location of GFP (Fig. 3A; Fig. S3C). Subsequently, we conducted a comprehensive assessment of DNA damage levels in NLS and NES cells, both in the presence and absence of TMZ treatment. We observed a pronounced increase in the level of phospho-γH2A in NES cells compared to NLS cells (Fig. 3B-G). This finding underscores the functional significance of nuclear-localized PGM2 in DNA damage repair mechanisms. Collectively, these results demonstrated that the nuclear localization is pivotal for the functional roles of PGM2 in DNA damage repair processes.

Earlier observations had noted the translocation of PGM2 into the nucleus in response to DNA damage induced by chemotherapeutic agents. In light of these insights, our pursuit to establish PGM2's direct involvement at DNA damage sites during repair led us to conduct DNA laser micro-irradiation assays in HeLa and U2OS cells expressing GFP or GFP-PGM2. The results conclusively revealed the rapid recruitment of PGM2 to the DNA damage site immediately following laser-induced DNA damage (405 nm), in stark contrast to GFP, which exhibited no such propensity for accumulation (Fig. 3H-K). These compelling observations substantiate the direct involvement of PGM2 in DNA damage repair processes, as it is precisely localized to sites of DNA damage. In conclusion, our comprehensive results highlight the unique and noncanonical role of nuclear PGM2 in the context of DNA damage repair, particularly its direct participation in the DNA damage repair process. These insights contribute to a deeper understanding of the functional mechanisms that govern PGM2-mediated DNA damage repair processes.

2.4. Phosphorylation of PGM2 at S165 protects cells against DNA damage stress

The intricate machinery of the DNA damage response (DDR) network depends on precisely coordinated protein phosphorylation dynamics. This process plays a pivotal role in regulating protein localization and their functional characteristics [16]. To further investigate the role of PGM2 in DNA damage repair, we engineered a Flag-PGM2 construct for flag beads immunoprecipitation to explore the phosphorylation state and potential interacting partners of PGM2. Subsequent to flag immunoprecipitation (flag-IP), mass spectrometry (MS) analysis unveiled the phosphorylation of PGM2 at the 165 serine (S165) site, a conservative site observed among various species (Fig. 4A). Notably, heightened phosphorylation levels were evident following etoposide treatment (Fig. S4C). To further investigate the role of PGM2 S165 phosphorylation, we generated mutant cell lines in which S165 was mutated to alanine (designated SA, a phospho-dead mutant) or aspartic acid (designated SD, a constant-phosphorylation mimic) in PGM2-knockout HeLa, U2OS and U251 cells (Figs. S4A and E). Intriguingly, these mutant lines exhibited no overt deviations in cellular localization patterns (Fig. S4B). We further observed a significant decrease in DNA damage in S165D cells compared to S165A cells. This finding was consistently confirmed through Western blot analysis and immunofluorescence staining targeting phospho-γH2A, highlighting the crucial role of PGM2 S165D in DNA damage repair (Fig. 4B-G; Fig. S4D). To investigate whether S165 phosphorylation plays a role in guiding PGM2's recruitment to DNA damage sites, we conducted DNA laser micro-irradiation assays. The results demonstrated the rapid and prominent recruitment of the S165D mutant to DNA damage sites, whereas the S165A mutant showed limited recruitment in HeLa, U2OS and U251 cells (Fig. 4H-K; Figs. S4F and G). In summary, our findings strongly support the notion that the phosphorylation status of PGM2 at serine 165 plays a crucial role in regulating its functional participation in DNA damage repair.

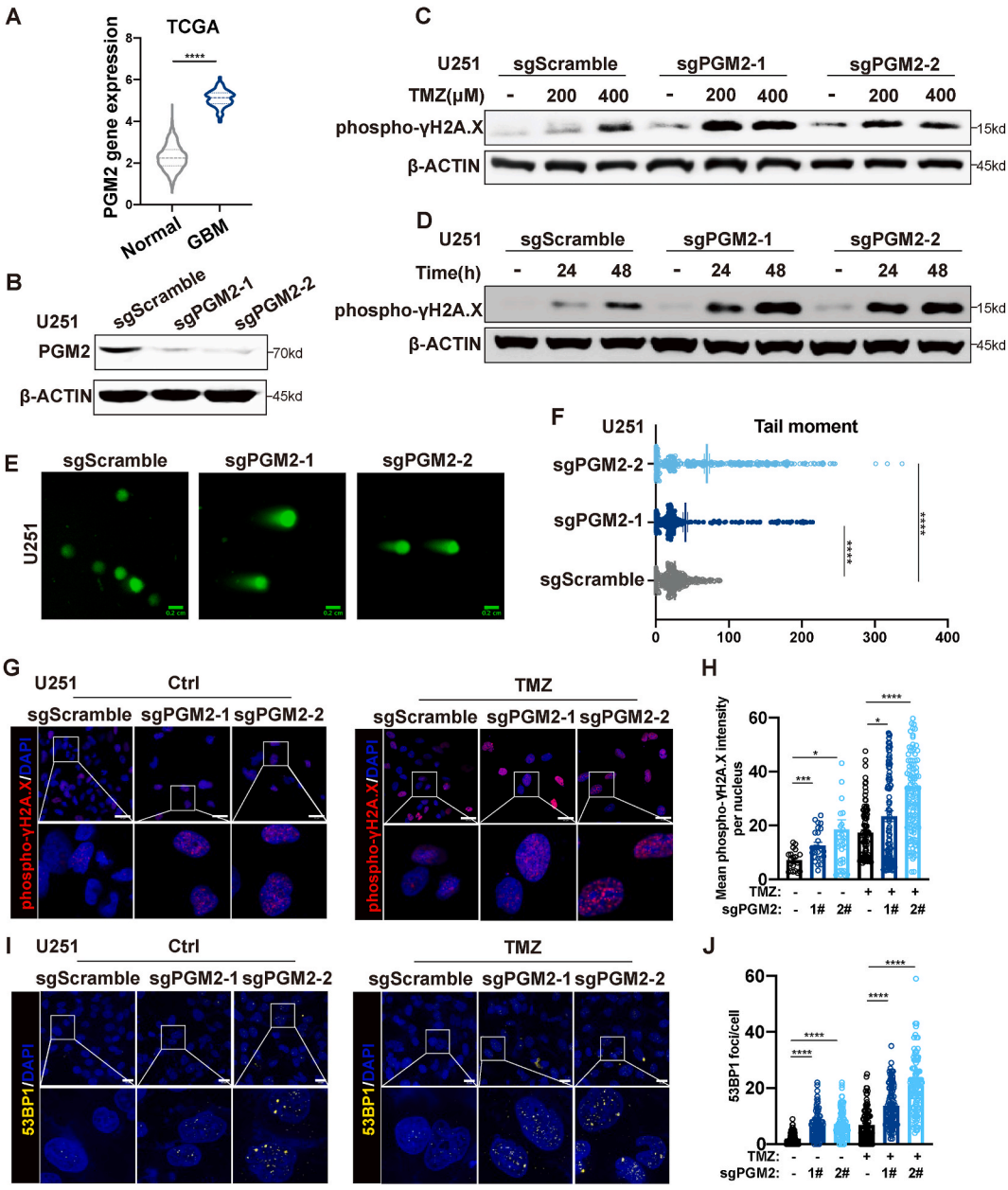

Fig. 2. PGM2 depletion enhances the sensitivity of GBM cells to DNA damage. A. The relative mRNA expression of PGM2 in TCGA and GTEx datasets. B. U251 cells were subjected to knockout of PGM2 using two independent sgRNAs, and the effectiveness of the knockout was confirmed through Western blot analysis. C. sgScramble and sgPGM2 U251 cells were treated with TMZ in a dose-dependent manner (0.001 % DMSO, TMZ 200 μM, 400 μM). DNA damage was assessed by quantifying phospho-γH2A.X protein levels. D. sgScramble and sgPGM2 U251 cells were treated with 0.001%DMSO or 400 μM TMZ in a time-dependent manner (24h, 48h). DNA damage was assessed by quantifying phospho-γH2A.X protein levels. E. U251 cells transfected with sgScramble or sgPGM2 were subjected to the neutral comet assay. Microphotographs representing the results of the neutral comet assay. Scale bar: 0.2 cm. F. Quantification of the tail moment of figure E. Data were compiled from approximately 100 cells in each group. G. Representative images of phospho-γH2A.X staining in U251 cells. Scale bar: 30 μm. U251 cells transfected with sgScramble or sgPGM2 were treated with 0.001 % DMSO or TMZ 400 μM for 48h, and after treatment, the level of phospho-γH2A.X was assessed through immunofluorescence staining. H. Quantification of phospho-γH2A.X intensity per nucleus of figure G. At least 50 cells were measured in each group. I. Representative images of TP53BP1 staining in U251 cells. Scale bar: 20 μm. U251 cells transfected with sgScramble or sgPGM2 were treated with 0.001 % DMSO or TMZ 400 μM for 48h, and after treatment, the level of TP53BP1 was assessed through immunofluorescence staining. J. Quantification of TP53BP1 foci per nucleus in figure I. At least 50 cells were counted in each group. Statistical significance was denoted as * for $p < 0.05$, ** for $p < 0.01$, *** for $p < 0.001$ and **** for $p < 0.0001$.

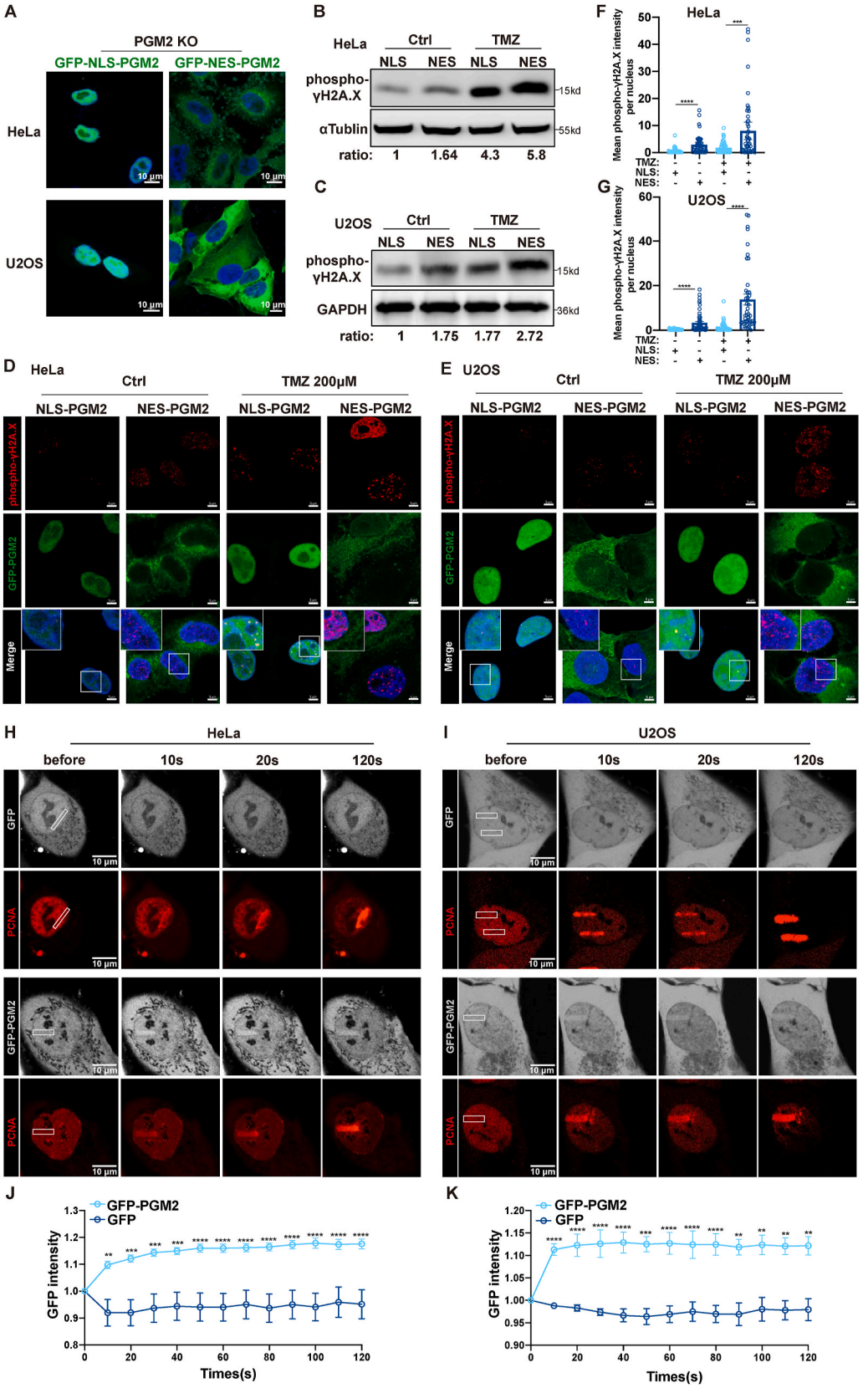

(caption on next page)

Fig. 3. Nuclear PGM2 is recruited to the DNA damage site. A. Immunofluorescence images displaying NLS- and NES-PGM2 in HeLa and U2OS sgPGM2 cells, with nuclei counterstained by DAPI. Scale bar: 10 μm. B. HeLa sgPGM2 cells were transfected with NLS- and NES-PGM2, followed by treatment with 0.001 % DMSO or 200 μM TMZ for 24 h. Then, the extent of DNA damage was evaluated by quantifying phospho-γH2A.X protein levels by WB. The levels of phospho-γH2A.X were measured using the DMSO-treated NLS group as the control. C. U2OS sgPGM2 cells were transfected with NLS- and NES-PGM2, followed by treatment with 0.001 % DMSO or 200 μM TMZ for 24 h. Subsequently, the extent of DNA damage was evaluated by quantifying phospho-γH2A.X protein levels by WB. The levels of phospho-γH2A.X were measured using the DMSO-treated NLS group as the control. D. Representative images showing phospho-γH2A.X and GFP-PGM2 in NLS- and NES-PGM2 HeLa sgPGM2 cells treated with 0.001 % DMSO or 200 μM TMZ for 24 h, with nuclei counterstained by DAPI. Scale bar: 5 μm. E. Representative images showing phospho-γH2A.X and GFP-PGM2 in NLS- and NES-PGM2 U2OS sgPGM2 cells treated with 0.001 % DMSO or 200 μM TMZ for 24 h, with nuclei counterstained by DAPI. Scale bar: 5 μm. F. Quantification of phospho-γH2A.X levels measured as mean intensity per nucleus in NLS- and NES-PGM2 sgPGM2 HeLa cells. At least 50 cells were measured in each group. G. Quantification of phospho-γH2A.X levels measured as mean intensity per nucleus in NLS- and NES-PGM2 sgPGM2 U2OS cells. At least 50 cells were measured in each group. H, I. Representative fluorescence micrographs of HeLa cells and U2OS cells expressing GFP or GFP-PGM2 individually coexpressing mCherry-PCNA as positive control, before and after laser micro-irradiation, following pretreatment with 10 μM BrdU for 24 h in HeLa cells and U2OS cells. Scale bar: 10 μm. J, K. Quantification of GFP intensity in the DNA laser micro-irradiation assay in Figure H, I. At least 10 cells were measured in each group. Statistical significance was denoted as * for $p < 0.05$, ** for $p < 0.01$, *** for $p < 0.001$, and **** for $p < 0.0001$.

2.5. ROCK2 interacts with PGM2

The intricate network of protein interactions governing DNA damage repair entails multifaceted complexities. Our experimental design of MS encompassed distinct conditions for flag-IP assays including the control group and etoposide-treated group, with a vector plasmid serving as the negative control (Fig. 5A; Fig. S5A). The conditions were carefully chosen to explore PGM2's possible interacting proteins during DNA damage response (Fig. S5B). Remarkably, distinct sets of proteins emerged across the experimental cohorts, with certain proteins consistently present in both groups. The results unveiled an intriguing candidate, ROCK2, which exhibited a heightened score in the etoposide-treated group compared to the control group (Fig. 5B). ROCK2, a serine/threonine kinase, plays critical roles in various cellular processes, including cytoskeletal organization, DNA damage repair, and cell cycle progression [17]. ROCK2 has been reported to interact with DNA repair assembly proteins to modulate the DDR, facilitating DNA damage repair in cancer cells [18–20]. To confirm the binding between ROCK2 and PGM2, we constructed PGM2 tagged with GFP-Flag and ROCK2 tagged with mRFP-HA, followed by co-immunoprecipitation (co-IP) experiments in 293T cells. The binding of PGM2 and ROCK2 was confirmed through flag immunoprecipitation and HA immunoprecipitation (Fig. 5C and D). Subsequently, semi-endogenous immunoprecipitation with HA in HeLa cells further confirmed the increased association between PGM2 and ROCK2 under etoposide treatment (Fig. 5E). Furthermore, the endogenous co-IP with PGM2 antibody revealed that the increased binding of ROCK2 and PGM2 under etoposide treatment in both HeLa and U251 cells (Fig. 5F; Fig. S5D). Building upon prior findings suggesting that the phosphorylation status of PGM2 at serine 165 played an important role in the DDR, we aimed to investigate whether this phosphorylation enhances its interaction with ROCK2. In both 293T, HeLa and U251 cells, we confirmed that ROCK2 specifically interacts with the PGM2 S165D mutant, in contrast to the S165A mutant (Fig. 5G and H; Fig. S5E). This observation consistently aligns with the functional differences observed between the S165A and S165D mutants. DNA laser micro-irradiation experiments further confirmed that knockdown of ROCK2 significantly hindered the recruitment of PGM2 to DNA damage sites, mirroring the behavior observed with the PGM2 S165A mutant (Fig. 5I and J, Figs. S5C and F-H). Taken together, this interaction emphatically highlights the pivotal role of the complex formed by phosphorylated PGM2 and ROCK2, which plays a key role in guiding PGM2's recruitment to DNA damage sites and, in turn, facilitates its active participation in DNA damage repair processes.

2.6. PGM2 knockdown sensitizes glioma to TMZ in vivo by activating the immune microenvironment

Previous research has uncovered the involvement of nucleotide metabolism and the DDR in modulating anti-tumor immune responses. We next investigate the role of PGM2 in anti-tumor immunity within immunocompetent murine. We utilized different shRNAs to achieve PGM2 knockdown in both GL261 and CT2A murine glioma cells, and the effectiveness of the knockdown was confirmed through qRT-PCR assessments (Fig. 6A; Fig. S6A). The increased DNA damage observed in PGM2 knockdown cells, both with and without TMZ treatment, aligned with previous results and was verified using immunofluorescence staining of phospho-γH2A.X (Fig. 6B and C). DNA damage is known for inducing the production of ISGs to amplify the immune response for enhanced anti-tumor immunity [21,22]. The heightened DNA damage, as a result, led to a robust generation of ISGs, which was confirmed through qRT-PCR. Notably, after exposure to TMZ, PGM2 knockdown cells displayed a significant increase in the upregulation of ISGs, including Cxcl10 and Ccl5 (Fig. 6F). The cyclic GMP–AMP synthase (cGAS)–stimulator of interferon genes (STING) pathway is an intrinsic immune pathway responsible for detecting both endogenous and exogenous double-strand DNA, thereby initiating a robust immune response [23,24]. The presence of micro-nuclei, indicative of DNA rupture and subsequent cGAS activation, was assessed in CT2A cells, revealing an elevated micro-nuclei level in the PGM2 knockdown groups (Fig. S6A).

For in vivo tumorigenesis assessment, we established mouse models using luciferase-expressing GL261 cells (GL261-luc). Notably, PGM2 knockdown significantly suppressed the growth of GL261-luc cells and increased their sensitivity to TMZ treatment, as evidenced by the luciferin intensity measurements (Fig. 6D and E). In both GL261 and CT2A glioma, knockdown of PGM2 greatly hindered the growth of glioma suggested by decreased tumor volume and improved survival (Fig. 6G; Fig. S6D). Moreover, we investigate the role of PGM2 in the regulation of the tumor microenvironment. The number of micro-nuclei in the shPGM2 cohort is significantly

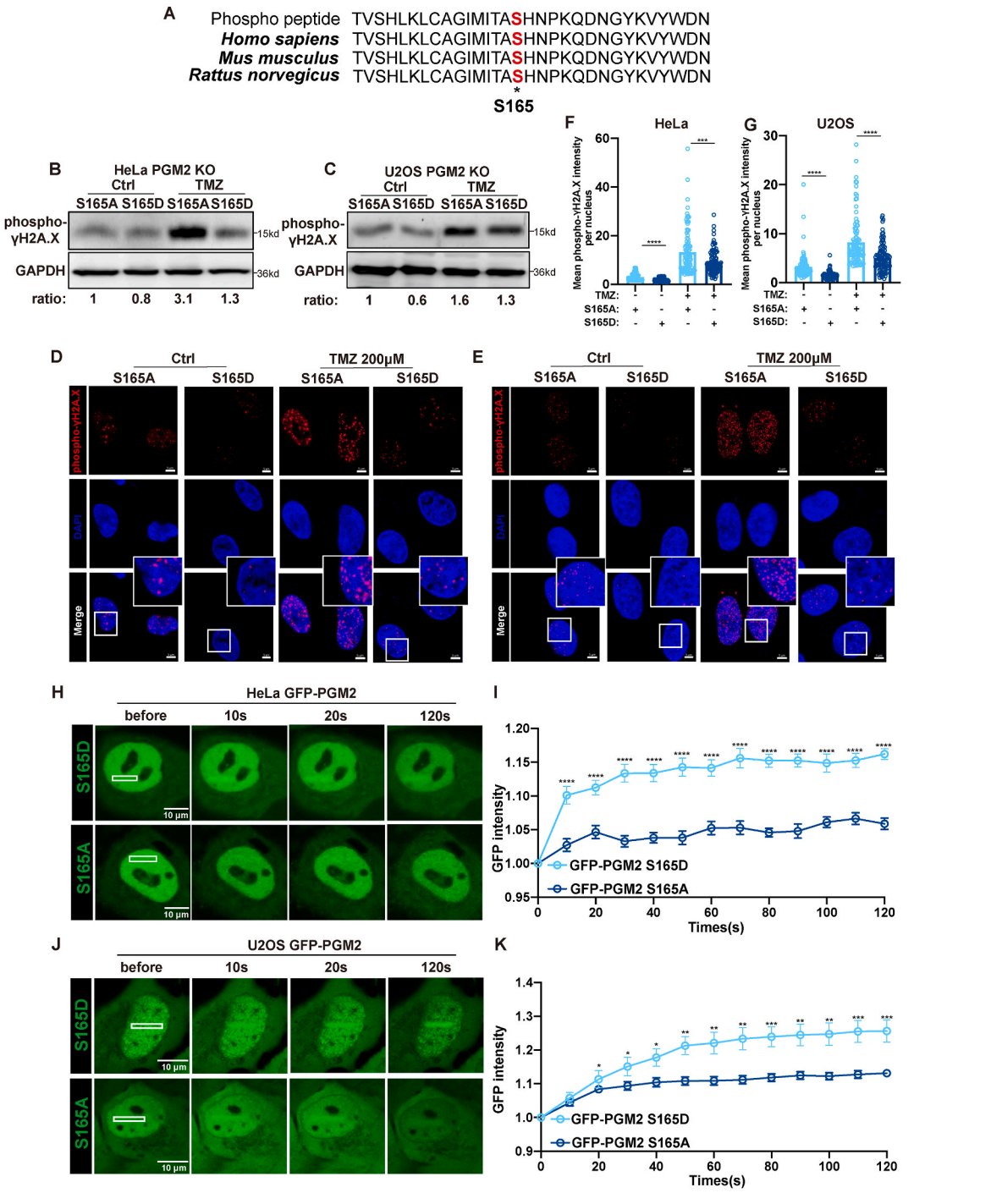

(caption on next page)

Fig. 4. Phosphorylation of PGM2 at S165 protects cells against DNA damage stress. A. The 165 serine phosphorylation site of PGM2 detected by MS is conservative. B. HeLa sgPGM2 cells were individually transfected with GFP-PGM2(S165A) and GFP-PGM2(S165D), followed by treatment with 0.001 % DMSO or 200 μM TMZ for 24 h. Subsequently, the extent of DNA damage was assessed by quantifying phospho-γH2A.X protein levels using Western blot analysis. The levels of phospho-γH2A.X were measured using the DMSO-treated S165A group as the control. C. U2OS sgPGM2 cells were individually transfected with GFP-PGM2(S165A) and GFP-PGM2(S165D), followed by treatment with 0.01 % DMSO or 200 μM TMZ for 24 h. Subsequently, the extent of DNA damage was assessed by quantifying phospho-γH2A.X protein levels using Western blot analysis. The levels of phospho-γH2A.X were measured using the DMSO-treated S165A group as the control. D. Representative images illustrating phospho-γH2A.X levels in PGM2 S165A and S165D HeLa sgPGM2 cells treated with 0.001 % DMSO or 200 μM TMZ for 24 h, with nuclei counterstained by DAPI. Scale bar: 5 μm. E. Representative images illustrating phospho-γH2A.X levels in PGM2 S165A and S165D U2OS sgPGM2 cells treated with DMSO or 200 μM TMZ for 24 h, with nuclei counterstained by DAPI. Scale bar: 5 μm. F. Quantification of phospho-γH2A.X levels measured as mean intensity per nucleus in Figure D. At least 50 cells were measured in each group. G. Quantification of phospho-γH2A.X levels measured as mean intensity per nucleus in Figure E. At least 50 cells were measured in each group. H. Representative fluorescence micrographs of HeLa cells individually expressing GFP-PGM2 S165A or GFP-PGM2 S165D, before and after laser micro-irradiation. Scale bar: 10 μm. I. Quantification of Figure H. At least 10 cells were measured in each group. J. Representative fluorescence micrographs of U2OS cells individually expressing GFP-PGM2 S165A or P-PGM2 S165D, before and after laser micro-irradiation. Scale bar: 10 μm. K. Quantification of Figure J. At least 10 cells were measured in each group. Statistical significance was indicated as * for $p < 0.05$, ** for $p < 0.01$, *** for $p < 0.001$, and **** for $p < 0.0001$.

higher than shScramble cohort (Fig. S6B), and immunofluorescence staining of frozen GL261 and CT2A glioma slices revealed a noticeable increase of $CD3^+$ cells, $CD8^+GranzB^+$ cells, and $CD8^+IFN\gamma^+$ cells within the shPGM2 cohort. This effect was further amplified when combined with TMZ treatment (Fig. 6H–M; Figs. S6I–S6J). In summary, PGM2 depletion led to increased production of ISGs and activation of immune cells, and sensitized glioma cells to TMZ treatment in vivo by activating the immune microenvironment.

2.7. ROCK2 inhibition sensitizes glioma to TMZ and PD-L1 in vivo by activating the immune microenvironment

Previous evidence has shown that the ROCK2-PGM2 complex plays an important role in DNA damage repair. Several ROCK inhibitors are currently undergoing clinical trials for diverse medical conditions, including diffuse cutaneous systemic sclerosis, chronic graft versus host disease (cGvHD), and Fuchs' endothelial dystrophy [25]. However, no prior study has explored the treatment potential of ROCK2 in glioma. As ROCK2 and ROCK1 share high homology, we selected the FDA-approved ROCK2-specific inhibitor Belumosudil (also known as KD025) to investigate its efficacy in treating glioma [17].

In both GL261 and CT2A glioma models, the inhibition of ROCK2 by Belumosudil (BEL) exhibited robust anti-tumor effects, either as a standalone therapeutic agent or in combination with TMZ treatment. This was evident through the reduction in tumor volume (Fig. 7A; Fig. S7C) and improved overall survival (Fig. 7B; Fig. S7D). Consistent with the results observed after PGM2 knockdown, treatment with Belumosudil also induced the activation of the immune microenvironment within the glioma, leading to increased numbers of $CD3^+$ cells, $CD8^+GranzB^+$ cells, and $CD8^+IFN\gamma^+$ cells (Fig. 7C-H; Figs. S7E–S7J). The cellular experiments further confirmed Belumosudil's ability to stimulate the expression of ISGs, and it demonstrated synergistic effects when combined with TMZ. Crucially, these effects were diminished when PGM2 was knocked down, implying that Belumosudil exerts its ISG-inducing function through PGM2 (Figs. S7A and B). Additionally, Belumosudil-treated groups exhibited an increased level of DNA damage in vivo (Figs. S7K and L).

Given the immune microenvironment activation within gliomas induced by pharmacological ROCK2 inhibition using Belumosudil, we aimed to combine Belumosudil with the immune checkpoint inhibitor PD-L1 to assess the potential sensitizing effect of ROCK2 inhibition on immunotherapy in glioma. The results demonstrate that Belumosudil sensitized PD-L1 treatment, led to reduced tumor volume (Fig. 7I), extended survival of mouse survival (Fig. 7J), and an increased presence of $CD3^+$ cells, $CD8^+GranzB^+$ cells, and $CD8^+IFN\gamma^+$ cells in the microenvironment (Fig. 7K–P). In conclusion, the pharmacological inhibition of ROCK2 using Belumosudil unequivocally demonstrates substantial anti-tumor effects characterized by increased DNA damage in cancer cells and concurrent activation of the immune microenvironment. This underscores the significant therapeutic promise of Belumosudil in the treatment of glioma.

3. Discussion

Cancer cells exhibit unique metabolic characteristics, especially in nucleotide metabolism that enable their rapid proliferation and resistance to treatment. In this study, we delved into the role of PGM2, an enzyme involved in the pentose phosphate pathway, within the context of DNA damage response in GBM.

The non-canonical role of metabolic enzymes revealed the dynamic crosstalk between cell metabolism and other important cellular processes. To meet the increased demands for materials required for DNA synthesis and DNA damage repair, cancer cells employ various strategies to meet their metabolic needs. One such strategy involves the upregulation of DNA-related metabolic enzymes to facilitate rapid material replenishment [4]. Besides fulfilling metabolic needs, the interaction between metabolic enzymes and DNA damage repair has gained growing attention in recent years. Multiple metabolic enzymes moonlight in DNA damage repair, including PKM2 [26], PGAM1 [12,27], and fructose-2,6- bisphosphatase 3 (PFKFB3) [28] by directly involved in the network of DDR [29]. PKM2 has been found to promote homologous recombination-mediated DNA double-strand break repair by phosphorylating and activating CtIP [26].

Our results demonstrate that PGM2 acquires a unique cellular location both in the cytoplasm and the nucleus, and its translocation

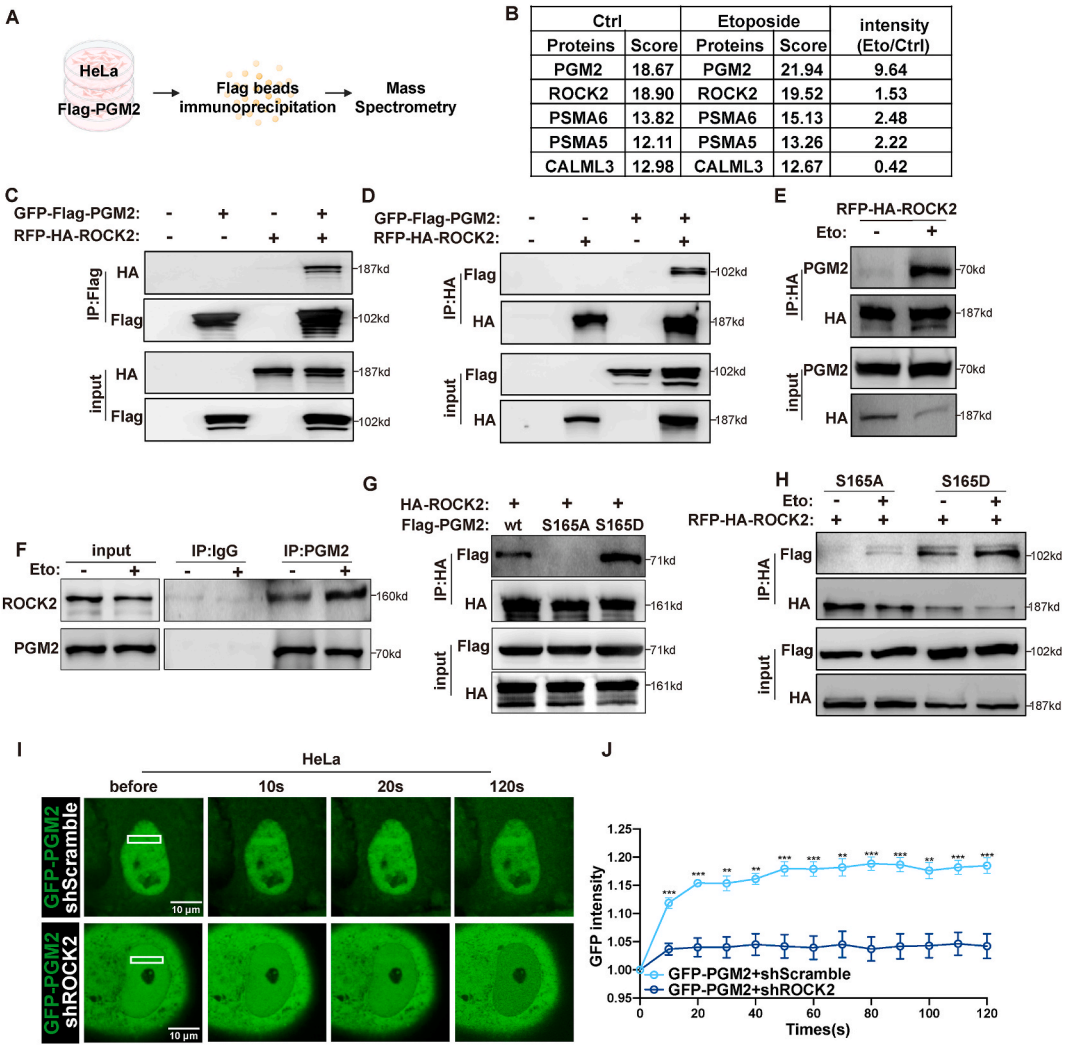

Ctrl		Etoposide		intensity
Proteins	Score	Proteins	Score	(Eto/Ctrl)
PGM2	18.67	PGM2	21.94	9.64
ROCK2	18.90	ROCK2	19.52	1.53
PSMA6	13.82	PSMA6	15.13	2.48
PSMA5	12.11	PSMA5	13.26	2.22
CALML3	12.98	CALML3	12.67	0.42

Fig. 5. ROCK2 interacts with PGM2. A. Workflow regarding flag beads immunoprecipitation of Flag-PGM2. B. Identification of potential interacting proteins in Ctrl and etoposide-treatment group. C. 293T cells were separately transfected with GFP-Flag-PGM2 and mRFP-HA-ROCK2 or co-transfected with both. After 36 h of transfection, cell lysates were immunoprecipitated using anti-Flag beads. The input and immunoprecipitates were subjected to immunoblotting for the indicated proteins. D. 293T cells were separately transfected with GFP-Flag-PGM2 and mRFP-HA-ROCK2 or co-transfected with both. After 36 h of transfection, cell lysates were immunoprecipitated using anti-HA beads. The input and immunoprecipitates were subjected to immunoblotting for the indicated proteins. E. HeLa cells expressing mRFP-HA-ROCK2 were treated with 0.001 % DMSO or 5 μM etoposide for 24 h. Cell lysates were immunoprecipitated using anti-HA beads. The input and immunoprecipitates were subjected to immunoblotting for the indicated proteins. F. HeLa cells were treated with 0.001 % DMSO or 5 μM etoposide for 24 h. Cell lysates were immunoprecipitated using the anti-PGM2 antibody or IgG control antibody. The input and immunoprecipitates were subjected to immunoblotting for the indicated proteins. G. 293T cells were separately transfected with Flag-PGM2 wt, S165A mutant, and S165D mutant together with mRFP-ROCK2. After 36 h of transfection, cell lysates were immunoprecipitated using anti-HA beads. The input and immunoprecipitates were subjected to immunoblotting for the indicated proteins. H. HeLa cells expressing mRFP-HA-ROCK2 separately with GFP-Flag-PGM2 S165A or S165D were treated with 0.001 % DMSO or etoposide 5 μM for 24h. Cell lysates were immunoprecipitated using anti-HA beads. The input and immunoprecipitates were subjected to immunoblotting for the indicated proteins. I. Representative fluorescence micrographs of HeLa cells stably expressing GFP-PGM2 with/without ROCK2 knock down in before and after DNA laser micro-irradiation assay. Scale bar: 10 μm. J. Quantification of DNA laser micro-irradiation assay in Fig. I. At least 10 cells were measured in each group. Statistical significance was indicated as * for $p < 0.05$, ** for $p < 0.01$, *** for $p < 0.001$, and **** for $p < 0.0001$.

into the nucleus occurs under DNA damage conditions. PGM2 depletion sensitizes GBM cells to DNA damage induced by chemotherapeutics. Our findings indicate that the translocation of PGM2 into the nucleus is linked to DNA damage repair, a process initiated by phosphorylation at the S165 site of PGM2. Furthermore, we have substantiated that the interaction between PGM2 and ROCK2 is crucial for PGM2's nuclear function. Notably, when we pharmacologically targeted ROCK2 using its inhibitor Belumosudil, we observed increased sensitivity of glioma to TMZ and PD-L1 treatments. The well-acknowledged role of ROCK2 is the direct phosphorylation of myosin light chain 2 (MLC2) to modulate the activity of myosin II. Besides its traditional roles in cell skeleton

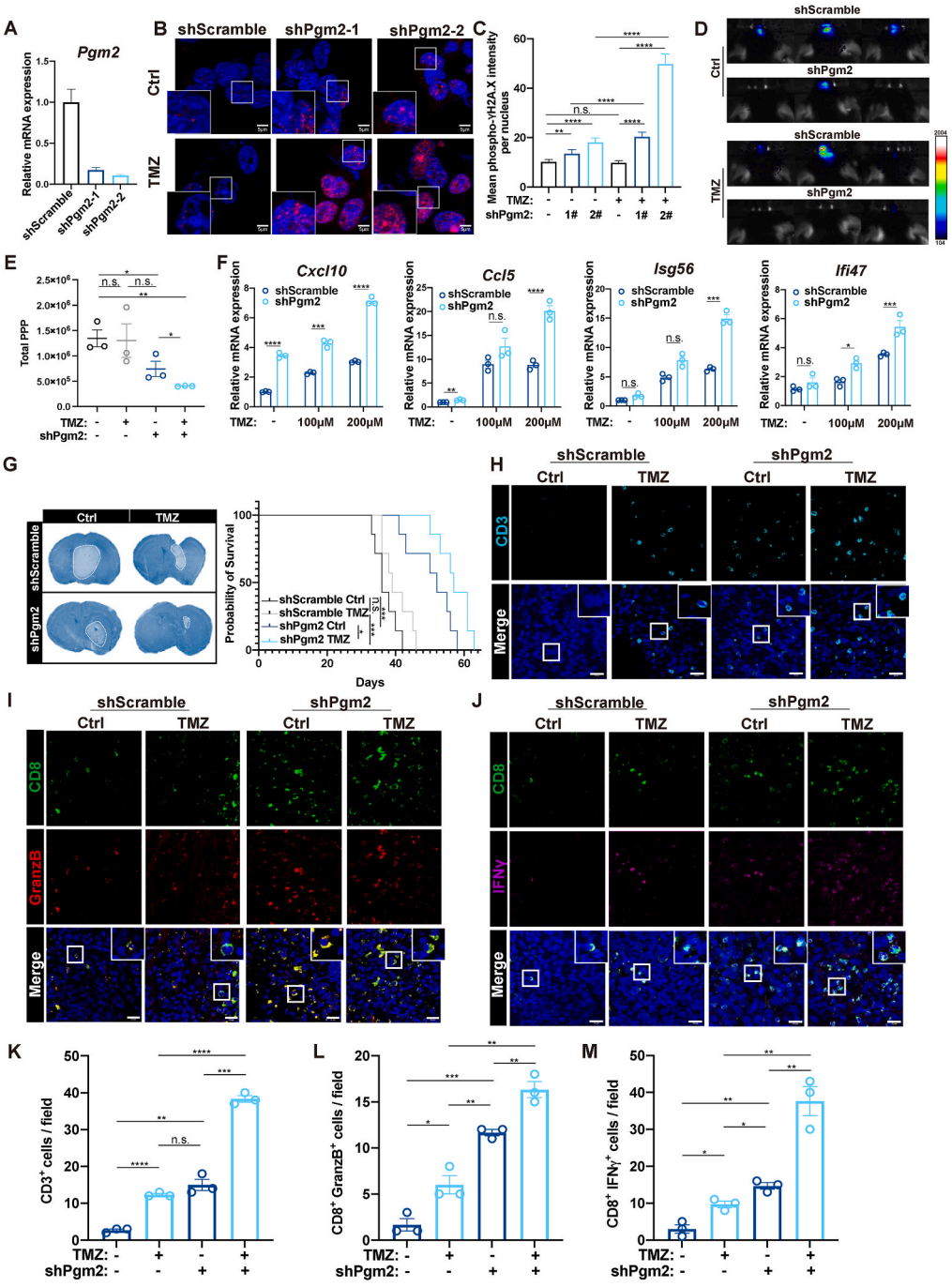

Fig. 6. PGM2 knockdown sensitizes glioma to TMZ in vivo by activating the immune microenvironment. A. Implementation of PGM2 knockdown in GL261 cells using two distinct shRNAs; effectiveness of the knockdown ascertained via qRT-PCR analysis. B. Display of representative phospho-γH2A.X stained GL261 cells expressing either scramble shRNA (shScramble), shPGM2-1, or shPGM2-2 with/without 400 μM TMZ treatment for 24h. Scale bar: 5 μm. C. Quantification of phospho-γH2A.X levels measured as mean intensity per nucleus in figure B. At least 50 cells were measured in each group. D. Representative bioluminescence imaging of C57/B6J mice bearing GL261-luc gliomas expressing either shScramble or shPGM2-2 with/without TMZ treatment. E. Quantitative assessment of the bioluminescent signal intensity in C57/B6J mice bearing GL261 gliomas expressing either shScramble or shPGM2-2 with/without TMZ treatment. F. Quantitative analysis of ISGs expression in CT2A cells expressing either shScramble or shPGM2-2 treated by 100 μM and 200 μM TMZ, performed via qRT-PCR. G. Representative brain slices image of GL261 glioma-bearing mice stained with DAPI for nuclear (Left panel). Kaplan-Meier survival analysis of C57/B6J mice intracranially implanted with GL261 cells expressing either shScramble or shPGM2-2 with/without TMZ treatment (Right panel). H. Fluorescence imaging of the distribution of $CD3^+$ from mice bearing GL261 gliomas expressing either shScramble or shPGM2-2 with/without TMZ treatment. Scale bar: 20 μm. I. Fluorescence imaging of $CD8^+GranzB^+$ cells within frozen sections from mice bearing GL261 gliomas expressing either shScramble or shPGM2-2 with/without

TMZ treatment. Scale bar: 20 μm. J. Fluorescence imaging of $CD8^+IFN\gamma^+$ cells within frozen sections from mice bearing GL261 gliomas expressing either shScramble or shPGM2-2 with/without TMZ treatment. Scale bar: 20 μm. K, L, M. Quantification of $CD3^+$ cells, $CD8^+GranzB^+$ cells, and $CD8^+IFN\gamma^+$ cells within fields of view of frozen sections from mice bearing GL261 gliomas expressing either shScramble or shPGM2-2 with/without TMZ treatment in Figure H, I, J. Three mice were counted in each group. Statistical significance was indicated as * for $p < 0.05$, ** for $p < 0.01$, *** for $p < 0.001$, and **** for $p < 0.0001$.

modulation, ROCK2 has been reported to bind with DDR proteins to participate in DNA damage repair [19], and in $MGMT^{low}$ glioma, ROCK2 is involved in homologous recombination repair to acquire temozolomide resistance [18]. Our study further proved the treatment potential of ROCK2 in GBM.

The nucleotide metabolism serves as an important bridge between cell metabolism and anti-tumor immunity. Targeting nucleotide metabolism rises as an effective strategy for enhancing cancer immunotherapy. Dihydroorotate dehydrogenase (DHODH), a key rate-limiting enzyme of pyrimidine biosynthesis, has been identified to efficiently treat various malignancies including GBM [5,6]. The DHODH inhibitor, P1788, has been found to enhance anti-tumor immunity through increased interferon signaling [30]. Targeting another rate-limiting enzyme, carbamoyl phosphate synthetase, aspartyl transcarbamoylase, and dihydroorotase (CAD), also increases the efficacy of immune checkpoint blockade therapy [31]. In our study, targeting PGM2 exhibited great potential in enhancing anti-tumor immunity by disrupting DNA damage response. The increased DNA damage induced the DNA sensing innate immune pathway cGAS-STING pathway activation and higher ISGs in the microenvironment, reshaping the immune environment and boosting anti-tumor immunity. Our research highlights the crosstalk between nucleotide metabolism and anti-tumor immunity. Targeting PGM2 directly by knockdown or indirectly by pharmacological inhibition of ROCK2 both showed significant treatment efficiency in GBM. In conclusion, we found that PGM2 participates in DNA damage response mediated by 165 serine phosphorylation and interaction with ROCK2. Hindering this process leads to increased DNA damage reshaping the immune microenvironment of glioma, enhancing the sensitivity to chemotherapy and immunotherapy (Fig. 7Q).

Despite these contributions, our study has certain limitations. To begin with, the signal that induced the phosphorylation of PGM2 and the details underlying its interaction with ROCK2 remain unclear. Also, the mechanisms regulating the translocation of PGM2 require further investigation. The recruitment of PGM2 onto the DNA damage site is rapid, requiring 165 serine phosphorylation and the interaction with ROCK2. However, the signal governing the nuclear translocation of PGM2 is so far unclear in our study. Additionally, the role of PGM2 in DNA damage repair also needs further investigation to identify the type of repair and interacting patterns of PGM2. The cytoplasmic and nuclear PGM2 presents slightly different molecular weight in the WB and this shift is not subjected to the phosphorylation. This indicates that PGM2 may have other modification during the DNA damage process and requires further investigation. Our study mainly focuses on in vitro and in vivo mouse models. More research is warranted to elucidate the broader implications of PGM2 in DDR across different contexts.

Materials and methods

Cell culture

The U251, HeLa, and U2OS cells were purchased from the Cell Resource Center of Shanghai Institute for Biological Sciences (Chinese Academy of Sciences, Shanghai, China). GL261 cells were kindly provided by Prof. Liufu Deng (Shanghai Jiao Tong University School of Medicine). GL261-luc cells were kindly provided by Prof. Linjie Zhao (Sichuan University) and CT2A cells were kindly provided by Prof. Chunsheng Kang (Tianjin Medical College). All the cells were cultured in DMEM medium (Meilunbio, Cat#MA0212) containing 10 % fetal bovine serum (Gibco, Cat#10270106) and 100 μg/ml of penicillin/streptomycin (Meilunbio, Cat#MA0110).

Western blotting

The same amounts of cells per group were collected and boiled with SDS-Page loading buffer. Electrophoresis was performed using 12 %, 10 %, or 8 % protein gels, followed by transfer onto PVDF membranes (Millipore). TBST supplemented with 3 % BSA was used for blocking for 1h at room temperature. Blotting with primary antibody (1:1000) was performed at 4 °C overnight. A secondary antibody (1:5000) was used to combine the primary antibody for 2 h. Finally, membranes were developed using an enhanced chemiluminescence detection system (Typhoon FLA 9500, GE Healthcare, Chicago, USA). Antibodies used in this study: PGM2 Polyclonal antibody, Proteintech, Cat#11022-1-AP; Phospho-Histone H2A.X (Ser 139) (20E3) Rabbit mAb, CST, Cat#9718; ROCK2 Monoclonal antibody, Proteintech, Cat#66633-1-Ig; HRP-conjugated HA Tag Recombinant antibody, Proteintech, Cat#HRP-81290; Monoclonal ANTI-FLAG® M2-Peroxidase (HRP) antibody produced in mouse, Sigma Aldrich, Cat#A8592; GFP-Tag (7G9) Mouse mAb, Abmart, Cat#M20004; Alpha Tubulin Monoclonal antibody, Proteintech, Cat#66031-1-Ig; Beta Actin Recombinant antibody, Proteintech, Cat#81115-1-RR; HRP-conjugated GAPDH Monoclonal antibody, Proteintech, Cat#HRP-60004; 53BP1 Antibody, CST, Cat#4937; HA-Tag (C29F4) Rabbit mAb, CST, Cat#3724; DYKDDDDK Tag (9A3) Mouse mAb, CST, Cat#8146; Lamin B1 Monoclonal antibody, Proteintech, Cat# 66095-1-Ig; HRP-conjugated Affinipure Goat Anti-Mouse IgG (H + L), Proteintech, Cat#SA00001-1; HRP-conjugated Affinipure Goat Anti-Rabbit IgG (H + L), Proteintech, Cat#SA00001-2.

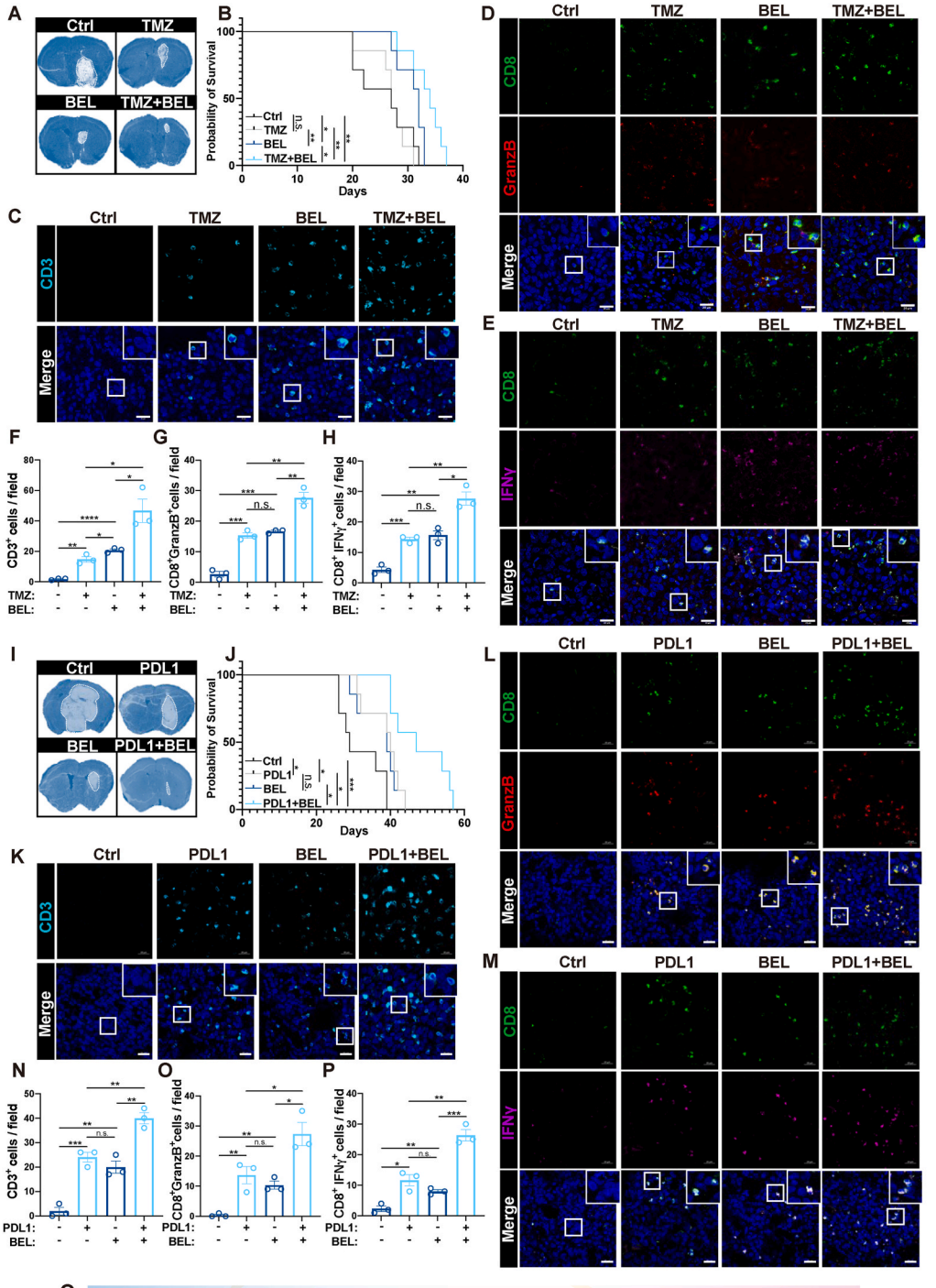

(caption on next page)

Fig. 7. ROCK2 inhibition sensitizes glioma to TMZ and PD-L1 in vivo by activating the immune environment. A. Representative brain slice image of GL261 glioma-bearing mice treated with TMZ, Belumosudil, or the combination of TMZ and Belumosudil stained with DAPI for nuclear. B. Kaplan-Meier survival analysis of C57/B6J mice intracranially implanted with GL261 cells treated with TMZ, Belumosudil, or the combination of TMZ and Belumosudil. C. Fluorescence imaging of the distribution of $CD3^+$ from mice bearing GL261 gliomas treated with TMZ, Belumosudil, or the combination of TMZ and Belumosudil. Scale bar: 20 μm. D. Fluorescence imaging of $CD8^+GranzB^+$ cells within frozen sections from mice bearing GL261 gliomas treated with TMZ, Belumosudil, or the combination of TMZ and Belumosudil. Scale bar: 20 μm. E. Fluorescence imaging of $CD8^+IFN\gamma^+$ cells within frozen sections from mice bearing GL261 gliomas treated with TMZ, Belumosudil, or the combination of TMZ and Belumosudil. Scale bar: 20 μm. F, G, H. Quantification of $CD3^+$ cells, $CD8^+GranzB^+$ cells, and $CD8^+IFN\gamma^+$ cells within fields of view of frozen sections from mice bearing GL261 glioma treated with TMZ, Belumosudil, or the combination of TMZ and Belumosudil in Figure C, D, E. Three mice were counted in each group. I. Representative brain slices image of GL261 glioma-bearing mice treated with PD-L1, Belumosudil, or the combination of PD-L1 and Belumosudil stained with DAPI for nuclear. J. Kaplan-Meier survival analysis of C57/B6J mice intracranially implanted with GL261 cells treated with PD-L1, Belumosudil, or the combination of PD-L1 and Belumosudil. K. Fluorescence imaging of the distribution of $CD3^+$ from mice bearing GL261 gliomas treated with PD-L1, Belumosudil, or the combination of PD-L1 and Belumosudil. Scale bar: 20 μm. L. Fluorescence imaging of $CD8^+GranzB^+$ cells within frozen sections from mice bearing GL261 glioma treated with PD-L1, Belumosudil, or the combination of PD-L1 and Belumosudil. Scale bar: 20 μm. M. Fluorescence imaging of $CD8^+IFN\gamma^+$ cells within frozen sections from mice bearing GL261 glioma treated with PD-L1, Belumosudil, or the combination of PD-L1 and Belumosudil. Scale bar: 20 μm. N, O, P. Quantification of $CD3^+$ cells, $CD8^+GranzB^+$ cells, and $CD8^+IFN\gamma^+$ cells within fields of view of frozen sections from mice bearing GL261 glioma treated with PD-L1, Belumosudil, or the combination of PD-L1 and Belumosudil. Three mice were counted in each group. Q. Diagrammatic representation of the non-canonical roles of PGM2 and the impact of PGM2 on glioma progression. Statistical significance was indicated as * for $p < 0.05$, ** for $p < 0.01$, *** for $p < 0.001$, and **** for $p < 0.0001$.

Immunofluorescence staining and imaging

For adherent cells immunofluorescence microscopy, cells were seeded into cover glasses in 12-well plates the night before treatment, and cells were treated accordingly the next day. At harvest time point, after washing with PBS two times, cells were fixed twice using 4 % paraformaldehyde (Biosharp, Cat#BL539A) for 30 min at room temperature and washed with PBS. Cells were then permeabilized with 0.01 % Triton X-100 for 10 min followed by PBS washing (3 × 5min), and blocked in 3 % bovine serum albumin (BSA) at room temperature for 30 min. Cells were incubated with primary antibodies (1:200) at 4 °C overnight. After washing with PBS three times, cells were then stained with the secondary antibody (1:500) conjugated with 488/594/647 fluorophore (Invitrogen) at 37 °C for 1 h. After washing PBS, nuclei were stained with DAPI. After adding the Fluoromount-G (SourthenBiotech, Cat#0100-01), the cells were viewed using confocal by Zeiss LSM900 microscope or Olympus FV3000 microscope. All imaging results were processed using ImageJ software from 560 NIH (Schneider et al., 2012).

For frozen tissue slice immunofluorescent staining, fix tissue by perfusing the animal with freshly prepared 4 % paraformaldehyde or by immersing it in 4 % paraformaldehyde for 4–24 h at room temperature. Cryoprotect the tissue by directly perfusing a sucrose solution or by first dissecting the tissue and allowing it to sink overnight in a 30 % sucrose/70 % fixative solution. Then embed tissue in OCT (Leica, Cat#020108926) cryostat sectioning medium and stored at −80 °C until ready for sectioning. Tissues were cut into 5–20 μm slices onto glass sides. The slides were washed in PBS twice followed by non-specific binding with 5 % normal donkey serum (Jackson ImmunoResearch, Cat#017-000-121) in PBST for 30 min at room temperature. The primary antibodies were added to the slides in 1 % serum PBST and incubated overnight at 4 °C in a humidified chamber. After washing with PBS twice, the secondary antibodies were added, and the slides were incubated at room temperature for 1–2 h. After washing PBS, nuclei were stained with DAPI. After adding the Fluoromount-G (SourthenBiotech), the slides were viewed using confocal by Zeiss LSM900 microscope or Olympus FV3000 microscope. All imaging results were processed using ImageJ software from 560 NIH (Schneider et al., 2012).

Antibodies used in this study: FITC anti-mouse CD3 Antibody, BioLegend, Cat#100204; FITC anti-mouse CD4 Antibody, BioLegend, Cat#100406; BD Horizon™ BB515 Rat Anti-Mouse CD8a, BD Horizon™, Cat#564422; PE/Dazzle™ 594 anti-human/mouse Granzyme B Recombinant Antibody, BioLegend, Cat#372216; BD Pharmingen™ PE Rat Anti-Mouse IFN-γ, BD Pharmingen™, Cat#554412; PerCP/Cyanine 5.5 anti-human/mouse Granzyme B Recombinant Antibody, BioLegend, Cat#372212.

Cell cycle blocking experiment

HeLa cells stably expressing green fluorescent protein (GFP) and GFP-PGM2 were seeded the day before the experiment in 12-well plates with coverslips for subsequent immunofluorescence and in 6 cm culture dishes for flow cytometry analysis of the cell cycle. The following day, drug treatments and releases were conducted at the specified time points as shown in the table below:

Day 1: At 9:00, cells were in asynchronous (Asyn) conditions. At 12:00, thymidine (Thy, Sigma, T0376) was added to the G1/S, S, and M phase samples. At 13:00, these cells were released (cells washed with PBS and culture medium replaced).

Day 2: At 9:00, thymidine was again added to the G1/S and S phase samples, and cells were released in the G2/M and M phases. At 12:00, cells in the G1/S, S, and M phases were released. At 13:00, cells in the G2/M phase were treated with Ro3306 (Selleck, S7747). At 17:00, cells in the G2/M and M phases were released. At 20:00, cells in the G2/M phase were treated with Ro3306 again. At 21:00, cells in the G2/M phase were released.

Day 3: At 9:00, all samples were in asynchronous conditions. At 12:00, the harvest was conducted for the G2/M phase cells.

Thy represents thymidine, with a working concentration of 5 μM. Ro3306 has a working concentration of 10 μM. Release refers to washing the cells twice with room temperature PBS, followed by replacing the medium with normal culture medium to continue cell culture. Samples were collected at 13:00 on Day 3 for immunofluorescence and flow cytometry analysis of the cell cycle.

Flow cytometry Cell cycle analysis

Cells were trypsinized to form a single-cell suspension, with digestion terminated by the addition of culture medium. The cells were resuspended in 200 μl PBS, and 500 μl ethanol was added to fix the cells on ice for 15 min. After fixation, cells were resuspended and washed twice with 1 ml PBS, centrifuging at 2000 rpm for 5 min each time. Subsequently, cells were stained on ice with 7-aminoactinomycin D 10 μM solution (beyotime, ST515) at a final concentration of 25 μg/ml for 10 min before performing flow cytometry analysis.

PGM2 gene expression plot

For the differential expression level of PGM2 in normal brain and GBM tissue, we downloaded the uniformly standardized pan-cancer dataset TCGA TARGET GTEx (PANCAN, N = 19131, G = 60499) from the UCSC database (https://xenabrowser.net/). From this dataset, we extracted the expression data for the gene ENSG00000169299 (PGM2) in Glioblastoma Multiforme (GBM). Additionally, we obtained human brain gene expression data from the GTEx database, focusing on the expression of PGM2 in normal brain tissue. Each expression value was subsequently transformed using log 2 (x+1). We then plotted the gene expression differences. The statistical significance of these differences was assessed using the Wilcoxon Rank Sum and Signed Rank Tests.

Co-immunoprecipitation (Co-IP)

For immunoprecipitation, the cells were washed with cold PBS and lysed in NP-40 buffer containing 50 mM Tris–HCl, 300 mM NaCl, 0.3 % NP-40, pH 7.4, PMSF and PI with rotation at 4 °C for 40 min. After centrifugation at 13,000g for 15 min at 4 °C, the supernatant was incubated with the indicated antibodies for 2 h, followed by incubation with Protein-A/G for another 1h at 4 °C. The precipitants were washed with wash buffer (20 mM Tris-HCl pH 8.0, 0.2 mM EDTA, 100 mM KCl, 2 mM MgCl2, 0.1 % Tween 20, 10 % glycerol) for 4 times, boiled with SDS sample buffer (50 mM Tris-HCl pH = 6.8, 2 % SDS, 10 % glycerol, 1 % β-mercaptoethanol, 0.1 % bromophenol blue) at 95 °C for 10 min and subjected to immunoblot analysis.

Nuclear/cytoplasmic fractionation separation

Cells were treated according to experimental design. Then cells were washed in ice-cold PBS, scraped from culture dishes on ice using a plastic cell scraper, and collected in 1.5 ml micro-centrifuge tubes in 1 mL of NP-40 buffer containing 50 mM Tris–HCl, 300 mM NaCl, 0.1 % NP-40, PMSF and PI. 300 μl of the cell-containing buffer was collected as the "whole-cell fraction (W)". Then the cells were centrifuged for 10 s in 1.5 ml micro-centrifuge tubes and 300 μl of the supernatant was removed as the "cytosolic fraction (C)". 100 μL of 4 × SDS Loading sample buffer was added to this fraction and boiled for 8 min. After the remaining supernatant was removed, the pellet was resuspended with 180 μL of 1 × SDS Loading buffer and designated as "nuclear fraction (N)". Nuclear fractions were sonicated using microprobes followed by boiling for 8 min.

Neutral comet assay

The neutral comet assay was performed following protocol from Jove [32]. Briefly, U251 cells expressing scramble, sgPGM2-1, and sgPGM2-2 were digested the cells and suspended cells at 2×10^5 cells/mL in 1 × PBS. Then, the cell suspension was combined with 1 % molten low melting point agarose (ThermoFisher, Cat#16520050) (at 37 °C) at a ratio of 1:10 (v/v) and immediately pipetted 30 μL onto a slide. Place the slide flat at 4 °C in the dark for 10 min. The slides were immersed in 4 °C lysis buffer in the dark for 1 h to overnight. Then the slides were immersed in a neutral electrophoresis buffer for 30 min at 4 °C followed by electrophoresis for 45 min at 4 °C. The slides were then merged in the DNA precipitation solution, followed by green fluorescent nucleic acid staining and image acquisition. Images were processed by the OpenComet plugin from Image J.

DNA laser micro-irradiation assay

HeLa cells or U2OS cells stably expressing GFP or GFP-PGM2 fusion protein were plated on 35 mm diameter glass-bottom plates at 1×10^5 cells/ml according to the experiment. The next day after transfection, cells were incubated with 10 μM 5-BrdU (beyotime, Cat#ST1056) overnight. Then, the cells were exposed to 10 μg/ml Hoechst 33342 (beyotime, Cat#C1022) for 10 min just before irradiation. Laser micro irradiation was performed with Olympus FV3000 confocal microscope and a 405 nm laser with 60 % energy. Relative intensity at laser-damaged sites was calculated as the mean value of the ratio of the intensity of each micro-irradiation-damaged site to the whole nucleus background. More than 10 individual cells were randomly chosen, tested, and analyzed for each data point.

Live cell imaging

HeLa cells or U2OS cells stably expressing GFP or GFP-PGM2 fusion protein were plated on 35 mm diameter glass-bottom plates at 1×10^5 cells/ml according to the experiment. On the next day, cells were treated with 20 μM etoposide (Selleck, Cat#S1225) for U2OS cells or 5 μM etoposide for HeLa cells and then placed on Olympus confocal. Images were requisite in 20-min intervals. Images were

analyzed by Olympus Oly software.

Live cell counting of cell death

U251 cells were seeded in a 48-well microplate the day before imaging. 24 h h later, DMSO and different doses of TMZ were added to U251 cells in the normal culture medium, including 2ug/L PI (Propidium Iodide). Then 48-well microplate was put in the Biotek Cytation™ 5 Cell Imaging Multi-Mode Reader. Imaging was started immediately following drug addition with a 4 × magnification objective using the 531/647 nm channel for the detection of PI-positive cells every 3 h. After 30 h of imaging acquisition, the image was processed, and PI-positive cells were counted at each time point by Gen 5 software.

Sample preparation for PGM2 phospho-proteomics and interacting protein MS

HeLa cells were seeded into three groups as the negative control, control, and etoposide-treated groups with three 10 cm dishes per group. After the indicated treatments, cells were washed by cold PBS twice and then lysed in NP-40 buffer containing 50 mM Tris–HCl, 300 mM NaCl, 0.3 % NP-40, pH 7.4, and protease inhibitor cocktail with rotation at 4 °C for 60 min. Then protein levels were measured by Nanodrop A280 then leveling of total protein between samples. 100ul flag beads per group were added into protein samples with rotation at 4 °C for 4 h. Centrifuge and remove the supernatant and wash the beads four times with lysis buffer. 3 × Flag peptide (beyotime, Cat#P9801) per-group was added to beads at with rotation at 4 °C overnight. Proteins were then reduced by 10 mM DTT at 37 °C for 1 h and alkylated by 20 mM IAA in the dark at 25 °C for 30 min. The lysates were then digested with trypsin at an enzyme/substrate ratio of 1:50 overnight at 37 °C. The enzyme digestion was terminated by adding the final concentration of formic acid to 5 percent, and the final samples were prepared for mass spectrometry analysis by desalting with a Waters' sepak desalting column. 100ug of protein was taken for high pH two-dimensional separation and the column was watered (BEH C18,300A, 1.7 μm, 2.1mmX150mm) to collect 20 fractions, which were finally combined into 4 fractions. We used Bruker nanoElute (Bruker Daltonics) liquid chromatography for the second dimension of the separation, using a 250 mm × 75 μm column (in opticks). Then all fractions were analyzed using a TIMS-TOF Pro mass spectrometer (Bruker Daltonics). The raw MS data were searched against the Swiss-Prot database (downloaded on August 20, 2020, containing 20375 protein sequence entries) using PEAKS Online Xpro Software (v1.4) for peptide and protein identifications and PTM identification was performed in PEAKS PTM searching module. Protein intensity is used for data analysis.

Quantitative RT-PCR

RNA purification kit (EZB, B0004DP) was used to isolate total cellular RNA from cell pellets. The 4 × EZscript Reverse Transcription Mix II with gDNA remover (EZB, RT2GQ) was used for reverse transcription into cDNA. Quantitative real-time PCR was performed using QuantStudio 6 Flex with 2 × S6 universal SYBR qPCR mix (NovaBio). Pairs of primers for qRT-PCR analyses used in this study were listed in Supplementary Table 1.

In vivo tumorigenesis

GL261 cells, GL261-luc cells, and CT2A cells were transduced with lentiviral vectors expressing shPGM2-2, or expressing a non-targeting control shRNA (shScramble) for the knockdown experiment. 48 h after infection, cells were examined by qRT-PCR for successful knockdown and then counted and engrafted intracranially into 6–8 weeks C57/B6J female mice. A burr hole was drilled into the skull of anesthetized C57BL/6 mice. Stereotactic coordinates were measured (2.0 mm lateral, and 2.0 mm anterior to the bregma). A burr hole was drilled at this point and relative cells suspended in 2.5 μl of PBS were injected through a syringe at a depth of 3.0 mm relative to the dura mater. Injections were performed at 1 μl/min. Then the needle was withdrawn, the bur hole was sealed with bone wax, and the incision sutured [33]. For GL261 cells, 5×10^4 cells were injected per mouse, and for GL261-luc and CT2A cells, 2×10^4 cells were injected per mouse. TMZ (Selleck, S1237), 20 mg/kg, was given intraperitoneally for five consecutive days from day 5 after glioma injection. Belumosudil (Selleck, S7936), 200 mg/kg, was given intraperitoneally for five consecutive days from day 5 after glioma injection. PD-L1 (InVivoMab, #BE0101), 200ug/mouse, was given intraperitoneally three times in two weeks from day 5 after glioma injection. On day 21 (for GL261 glioma models) or day 14 (for CT2A glioma models), three random mice in each group were sacrificed for brain harvest, followed by frozen slice staining for indicated antibodies.

Animals were maintained until neurological signs were apparent, at which point they were sacrificed. Brains were collected and fixed in 4 % paraformaldehyde, paraffin-embedded, and then sectioned. Sections were stained with hematoxylin and eosin for histological analysis. In parallel survival experiments, animals were monitored until they developed neurological signs.

In vivo bioluminescence analysis

To monitor tumor growth in living mice, GL261-luc cells expressing shScramble, shPGM2-1, and shPGM2-2 were transduced with firefly luciferase through lentiviral infection. 48 h after shRNA infection, 2×10^4 GL261-luc cells were intracranially transplanted into C57/B6J mice. Then, mice were intraperitoneal injected with 120 mg/kg D-luciferin (Gold Bio-tech, Cat#40901 ES) and anesthetized with isoflurane on the indicated days. The size of the tumor was monitored by the bioluminescence channel of the IVIS Spectrum imaging system.

Statistics and reproducibility

Analytical computations were carried out utilizing GraphPad Prism (version 9.0) and Microsoft Excel (OFFICE 2021). Comprehensive interpretations of data underpinning the statistical examinations along with precise P values can be found in the Source Data. Specific details of each experiment's statistical assessments are included in the figure captions. A two-tailed Student's t-test was routinely employed for paired comparisons, and either one-way or two-way ANOVA was used for multi-variate comparisons. Unless otherwise noted, the presented data embodies outcomes of three independent experiments, reported as the mean ± standard deviation or standard error of the mean. A P value less than 0.05 was set as the threshold for statistical significance. The sample size was not predetermined by a statistical method, and no data was eliminated from the computations. qRT–qPCR was conducted with three biological replicates, except where indicated otherwise in the figure descriptions. Western blot analysis was repeated twice with analogous outcomes; a representative blot from these two independent tests is displayed.

Ethical approval

All mice experiments were performed under an animal protocol approved by the Institutional Animal Care and Use Committee of the Shanghai Medical College, Fudan University (Number: 202311005Z).

CRediT authorship contribution statement

Yingying Lyu: Writing – review & editing, Writing – original draft, Visualization, Validation, Methodology, Investigation, Conceptualization. **Chaxian Liu:** Writing – review & editing, Validation, Investigation, Formal analysis, Data curation, Conceptualization. **Hao Lin:** Writing – review & editing, Validation, Investigation, Formal analysis, Data curation. **Haikun Song:** Visualization, Validation, Investigation, Conceptualization. **Qiyuan Zhuang:** Writing – review & editing, Conceptualization. **Ankang Hu:** Conceptualization. **Liang Chen:** Supervision, Project administration, Conceptualization. **Hui Yang:** Writing – review & editing, Supervision, Resources, Project administration, Methodology, Funding acquisition, Data curation, Conceptualization. **Ying Mao:** Writing – review & editing, Supervision, Resources, Project administration, Funding acquisition, Data curation, Conceptualization.

Declaration of competing interest

The authors declare the following financial interests/personal relationships which may be considered as potential competing interests:Ying Mao reports financial support was provided by National Key Research and Development Program of China. Hui Yang reports financial support was provided by National Natural Science Foundation of China. Ying Mao reports financial support was provided by Shanghai Municipal Science and Technology Major Project. Hui Yang reports financial support was provided by Program for Professor of Special Appointment Eastern Scholar at Shanghai Institutions of Higher Learning. If there are other authors, they declare that they have no known competing financial interests or personal relationships that could have appeared to influence the work reported in this paper.

Acknowledgments

This work is supported by the National Key Research and Development Program of China (No. 2020YFA0804200), NSFC grant (No. 82073166, 82273203), and Shanghai Municipal Science and Technology Major Project (No.2018SHZDZX01). H.Y. is supported by the Program for Professors of Special Appointment (Eastern Scholar) at the Shanghai Institutions of Higher Learning (Grant SSF151005).

Appendix A. Supplementary data

Supplementary data to this article can be found online at https://doi.org/10.1016/j.heliyon.2024.e36415.

References

[1] S.L. Rocha Pinheiro, et al., Immunotherapy in glioblastoma treatment: current state and future prospects, World J. Clin. Oncol. 14 (4) (2023) 138–159.
[2] M. Lim, et al., Current state of immunotherapy for glioblastoma, Nat. Rev. Clin. Oncol. 15 (7) (2018) 422–442.
[3] P.P. Hsu, D.M. Sabatini, Cancer cell metabolism: warburg and beyond, Cell 134 (5) (2008) 703–707.
[4] N.J. Mullen, P.K. Singh, Nucleotide metabolism: a pan-cancer metabolic dependency, Nat. Rev. Cancer 23 (5) (2023) 275–294.
[5] D.D. Shi, et al., De novo pyrimidine synthesis is a targetable vulnerability in IDH mutant glioma, Cancer Cell 40 (9) (2022) 939–956.e16.
[6] S. Pal, et al., A druggable addiction to de novo pyrimidine biosynthesis in diffuse midline glioma, Cancer Cell 40 (9) (2022) 957–972.e10.
[7] D.D. Shi, et al., Emerging roles of nucleotide metabolism in cancer, Trends Cancer 9 (8) (2023) 624–635.
[8] W. Zhou, et al., Purine metabolism regulates DNA repair and therapy resistance in glioblastoma, Nat. Commun. 11 (1) (2020) 3811.
[9] C.J. Halbrook, et al., Macrophage-released pyrimidines inhibit gemcitabine therapy in pancreatic cancer, Cell Metabol. 29 (6) (2019) 1390–1399.e6.
[10] C. Pan, B. Li, M.C. Simon, Moonlighting functions of metabolic enzymes and metabolites in cancer, Mol Cell 81 (18) (2021) 3760–3774.
[11] M.R. Hara, et al., S-nitrosylated GAPDH initiates apoptotic cell death by nuclear translocation following Siah 1 binding, Nat. Cell Biol. 7 (7) (2005) 665–674.

[12] J. Qu, et al., Phosphoglycerate mutase 1 regulates dNTP pool and promotes homologous recombination repair in cancer cells, J. Cell Biol. 216 (2) (2017) 409–424.
[13] W. Yang, et al., PKM2 phosphorylates histone H3 and promotes gene transcription and tumorigenesis, Cell 158 (5) (2014) 1210.
[14] K.C. Patra, N. Hay, The pentose phosphate pathway and cancer, Trends Biochem. Sci. 39 (8) (2014) 347–354.
[15] P. Maliekal, et al., Molecular identification of mammalian phosphopentomutase and glucose-1,6-bisphosphate synthase, two members of the alpha-D-phosphohexomutase family, J. Biol. Chem. 282 (44) (2007) 31844–31851.
[16] F.J. Groelly, et al., Targeting DNA damage response pathways in cancer, Nat. Rev. Cancer 23 (2) (2023) 78–94.
[17] J. Barcelo, R. Samain, V. Sanz-Moreno, Preclinical to clinical utility of ROCK inhibitors in cancer, Trends Cancer 9 (3) (2023) 250–263.
[18] X. Zhang, et al., Acquired temozolomide resistance in MGMT(low) gliomas is associated with regulation of homologous recombination repair by ROCK2, Cell Death Dis. 13 (2) (2022) 138.
[19] A. Pranatharthi, et al., RhoC regulates radioresistance via crosstalk of ROCK2 with the DNA repair machinery in cervical cancer, J. Exp. Clin. Cancer Res. 38 (1) (2019) 392.
[20] C. Cheng, et al., Role of small GTPase RhoA in DNA damage response, Biomolecules 11 (2) (2021).
[21] T. Reisländer, F.J. Groelly, M. Tarsounas, DNA damage and cancer immunotherapy: a STING in the tale, Mol Cell 80 (1) (2020) 21–28.
[22] H. Cheon, et al., How cancer cells make and respond to interferon-I, Trends Cancer 9 (1) (2023) 83–92.
[23] S. Yum, M. Li, Z.J. Chen, Old dogs, new trick: classic cancer therapies activate cGAS, Cell Res. 30 (8) (2020) 639–648.
[24] N. Samson, A. Ablasser, The cGAS-STING pathway and cancer, Nat Cancer 3 (12) (2022) 1452–1463.
[25] N. Koizumi, et al., New therapeutic modality for corneal endothelial disease using Rho-associated kinase inhibitor eye drops, Cornea 33 (Suppl 11) (2014) S25–S31.
[26] S.T. Sizemore, et al., Pyruvate kinase M2 regulates homologous recombination-mediated DNA double-strand break repair, Cell Res. 28 (11) (2018) 1090–1102.
[27] S. Ohba, et al., Phosphoglycerate mutase 1 activates DNA damage repair via regulation of WIP1 activity, Cell Rep. 31 (2) (2020) 107518.
[28] N.M.S. Gustafsson, et al., Targeting PFKFB3 radiosensitizes cancer cells and suppresses homologous recombination, Nat. Commun. 9 (1) (2018) 3872.
[29] D. Xu, et al., The evolving landscape of noncanonical functions of metabolic enzymes in cancer and other pathologies, Cell Metabol. 33 (1) (2021) 33–50.
[30] S. Hayek, et al., Cerpegin-derived furo[3,4-c]pyridine-3,4(1H,5H)-diones enhance cellular response to interferons by de novo pyrimidine biosynthesis inhibition, Eur. J. Med. Chem. 186 (2020) 111855.
[31] H.F. Tu, et al., Afatinib exerts immunomodulatory effects by targeting the pyrimidine biosynthesis enzyme CAD, Cancer Res. 81 (12) (2021) 3270–3282.
[32] Y. Au - Lu, Y. Au - Liu, C. Au - Yang, Evaluating in vitro DNA damage using comet assay, JoVE (128) (2017) e56450.
[33] J.H. Park, et al., Protocol to analyze antitumor immunity of orthotopic injection and spontaneous murine high-grade glioma models using flow cytometry and single-cell RNA sequencing, STAR Protoc 3 (3) (2022) 101607.